

# *Damage and plastic deformation of reservoir rocks: Part 2. Propagation of a hydraulic fracture*

**Seth Busetti, Kyran Mish, Peter Hennings, and Ze'ev Reches**

## **ABSTRACT**

The aim of part 2 is to understand the development of complex hydraulic fractures (HFs) that are commonly observed in the field and in experiments but are not explained by most models. Our approach uses finite element simulations and a numerical rheology developed in part 1 to model damage fracturing, the fracturing process by damage propagation in a rock with elastic–plastic damage rheology. Using this rheology and a dynamic solution technique, we investigate the effect of far-field stresses and pressure distribution in the fracture on the geometric complexity of the fractures.

The model is for the vertical propagation of an HF segment into an overlying bed located far from borehole effects. The layer is 2.3 m (7.5 ft) tall, has elastic–plastic damage rheology, and contains a 0.3-m (1-ft)–tall initial vertical fracture. Vertical and horizontal tectonic loads of 50 MPa (7252 psi) and 10 to 45 MPa (1450–6527 psi) are established, and then an internal fracture pressure of 10 MPa/s (1450 psi/s) is applied until the layer fails. The simulated fracturing is sensitive to the stress state and generated patterns range from single straight fractures to treelike networks. Reducing differential stress increases the injection pressure required to fracture and promotes off-plane damage, which increases fracture complexity. Consecutive periods of nonuniform weakening followed by unstable rupture generate multiple branches and segments.

## **AUTHORS**

**SETH BUSETTI** ~ *ConocoPhillips School of Geology and Geophysics, University of Oklahoma, 100 East Boyd Street Suite 710, Norman, Oklahoma; present address: ConocoPhillips Subsurface Technology, 600 North Dairy Ashford, Houston, Texas; seth.busetti@conocophillips.com*

Seth Busetti received his B.S. degree in geological engineering from the Colorado School of Mines and his M.S. degree and Ph.D. in structural geology from the University of Oklahoma. Busetti is currently employed at ConocoPhillips and works in a subsurface technology position focusing on applied structural geology and geomechanics problems worldwide. He is currently involved in projects involving fracture and fault mechanics, fluid flow in fractured reservoirs, and geomechanics in nonconventional reservoirs.

**KYRAN MISH** ~ *School of Civil Engineering and Environmental Science, University of Oklahoma, 202 West Boyd Street Room 334, Norman, Oklahoma; present address: Sandia National Laboratories, P.O. Box 5800, MS-0932, Albuquerque, New Mexico; kdmish@sandia.gov*

Kyran Mish received his B.S. degree in mathematics, his M.S. degree in structural mechanics, and his Ph.D. in engineering, all from the University of California at Davis. Before his present position at Sandia National Laboratories, Mish was in management at Lawrence Livermore National Laboratory, served on the faculty of University of California at Davis and, most recently, was the director of the Donald G. Fears Structural Engineering Laboratory and a professor of structural engineering at the University of Oklahoma.

**PETER HENNINGS** ~ *ConocoPhillips Subsurface Technology, 600 North Dairy Ashford, Houston, Texas; peter.hennings@conocophillips.com*

Peter Hennings received his B.S. and M.S. degrees in geology from the Texas A&M University and his Ph.D. in geology from the University of Texas. He has held various technical supervisory positions in Mobil Research Company, Phillips Petroleum Company, and ConocoPhillips. He is currently the manager of the Structure and Geomechanics group in ConocoPhillips Subsurface

---

Copyright ©2012. The American Association of Petroleum Geologists. All rights reserved.

Manuscript received January 27, 2011; provisional acceptance July 1, 2011; revised manuscript received September 9, 2011; revised provisional acceptance November 28, 2011; 2nd revised manuscript received January 3, 2012; final acceptance February 1, 2012.

DOI:10.1306/02011211011

Technology. He is a former AAPG Distinguished Lecturer, a Geological Society of America Honorary Fellow, and is an adjunct professor at the University of Wyoming and Stanford University.

ZE'EV RECHES ~ *ConocoPhillips School of Geology and Geophysics, University of Oklahoma, 100 East Boyd Street Suite 710, Norman, Oklahoma; reches@ou.edu*

Ze'ev Reches received his B.S. and M.S. degrees in geology from Hebrew University, Israel, and his Ph.D. in structural geology from Stanford University, California. Reches serves as a professor of structural geology at the University of Oklahoma. His previous work includes positions at Arizona State University, Stanford University, and the U.S. Geological Survey at Menlo Park, California, and Hebrew University, Israel. His research interests include earthquake and fault processes and rock mechanics.

## ACKNOWLEDGEMENTS

The funding and resources for this project came from the ConocoPhillips School of Geology and Geophysics and the School of Civil Engineering and Environmental Science at the University of Oklahoma, Devon Energy, and ConocoPhillips. We thank Vincent Heesakkers, Tricia Allwardt, Jean-Claude Roegiers, Leonid Germanovich, Ray Fletcher, Jeff Kelly, and John Daniels for the discussions that benefited this work. We also thank Jeff Hall and Herb Magley at Devon Energy for generously providing Barnett Shale field and operational data. Finite element simulations were conducted using the academic version of the code Abaqus (a product of Simulia, a division of Dassault Systemes). We found the reference material in the digital Abaqus manual to be very helpful. We thank the two manuscript reviewers whose comments and recommendations were most invaluable.

The AAPG Editor thanks the anonymous reviewers for their work on this paper.

We find that the processes that form HF complexity occur under a range of in-situ reservoir conditions and are likely to contribute to complex far-field fracture geometry and enhanced network connectivity.

## INTRODUCTION

Hydraulic fractures in the crust commonly display complex shapes with multiple interconnected segments, bridging branches, and rupture-arrest structures (Figure 1; Delaney et al., 1986; Weinberger et al., 2000; Sagy et al., 2001). These structures indicate that fracture propagation in rocks is a complex process with local interactions, widespread damage, brittle failure, and dynamic stress changes. This complexity is not addressed in the classical fracture mechanics models that typically predict the formation of a single simple fracture (Hubbert and Willis, 1957; Irwin, 1958; Barenblatt, 1962). The main objective here is to investigate hydraulic fracture propagation in rocks while using a rheological model that is based on rock mechanics experimental data.

We developed this rheological model in part 1 (Busetti et al., 2012) by incorporating the dominant deformation modes of rocks into a numerical elastic-plastic damage model. The analysis was conducted with the Abaqus finite element (FE) program. We refined and calibrated the numerical rheology using experimental data for Berea Sandstone, a typical analog of reservoir rocks (e.g., Hart and Wang, 1995; Menendez et al., 1996). Two experimental configurations were used for the model calibration: four-point beam (Weinberger et al., 1994) and dogbone triaxial (Ramsey and Chester, 2004; Bobich, 2005). Both of these configurations generate local tensile conditions under global confining pressure, which are expected close to a hydraulic fracture (HF). The numerical analyses successfully simulated damage distribution and fracture patterns of the experiments (part 1), and we thus concluded that the derived rheology is a realistic modeling tool for in-situ deformation of Berea-like reservoir rocks (details in part 1).

The three central features of the present analysis are (1) implementation of the elastic-plastic damage rheology developed in part 1, (2) using local damage distribution as an indicator of fracture propagation path, and (3) using dynamic solution techniques to explore fracture propagation dynamics. We explore the effects of loading conditions on fracture morphology at the tip of a pressurized HF within a layer, focusing on the effect of the HF pressure and tectonic stress on the fracture complexity and morphology. The simulations

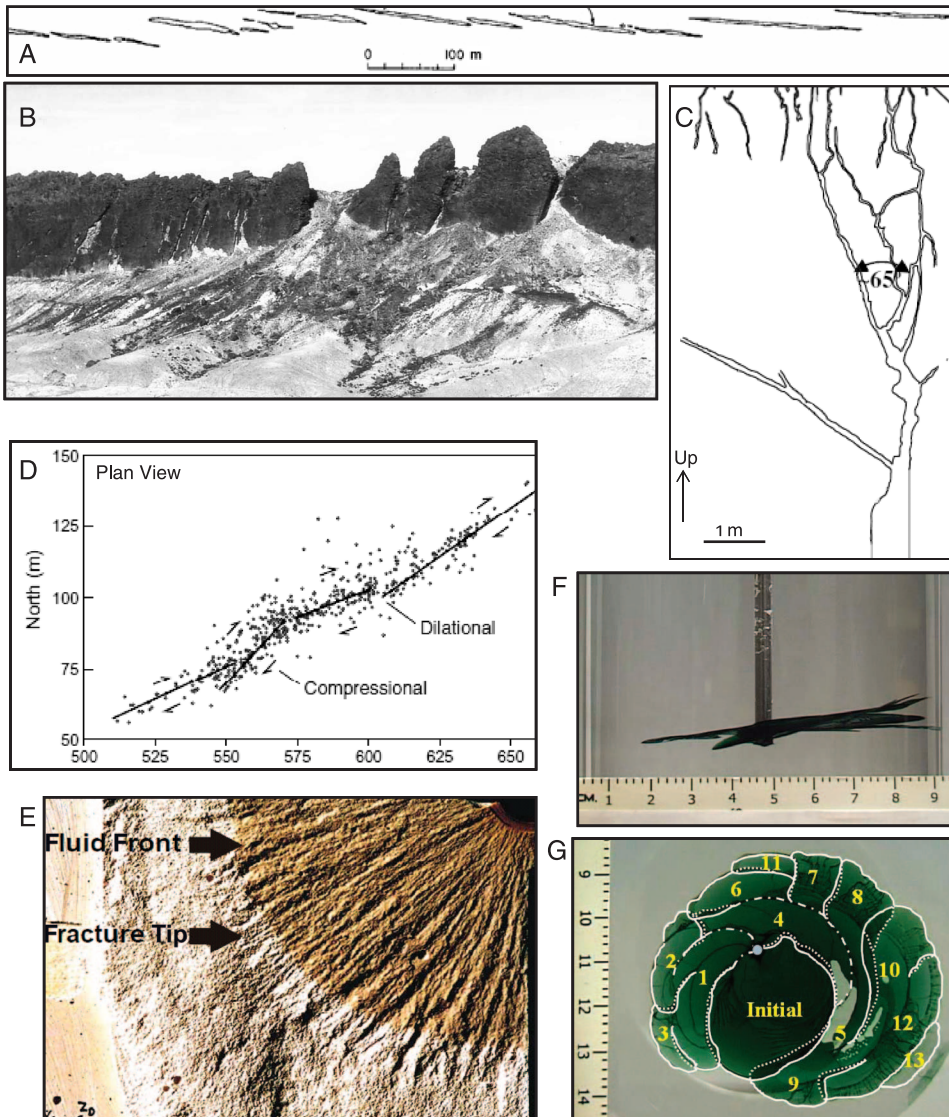


**Figure 1.** Examples of complex hydraulic fracture morphology. (A) Map view of dike segments near Ship Rock, New Mexico (Pollard, 1978). (B) Oblique view of dike segments near the San Rafael swell, Utah (Delaney and Gartner, 1997; used with the permission of the Geological Society of America). (C) Upward-branching clastic dike in the Amí'az Plain, Dead Sea Basin (Levi et al., 2009; used with the permission of the Journal of Structural Geology). (D) Hydraulic fracture jogs interpreted from mapped microseismicity in the Carthage Cotton Valley gas field, Texas (Rutledge et al., 2004; used with permission of the Seismological Society of America). (E) Grooved fracture surface and fluid lag region from laboratory hydraulic fracture experiments (Papanastasiou, 2002). (F) Side view and (G) top view of out-of-plane segments and asymmetric lobes in a flower petal hydraulic fracture in polymethyl methacrylate (PMMA) (Wu, 2006).

suggest that the simple fractures predicted by basic hydraulic fracturing models (e.g., Hubbert and Willis, 1957) may develop under a limited range of field conditions. However, under general reservoir conditions, the simulations show that segments, bridges, branches, and rupture-arrest features are generated spontaneously by damage fracturing. We propose that these simulations can be applied to hydrocarbon reservoirs in which production HF's are best explained as fracture networks with multiple fractures (Busetti, 2009).

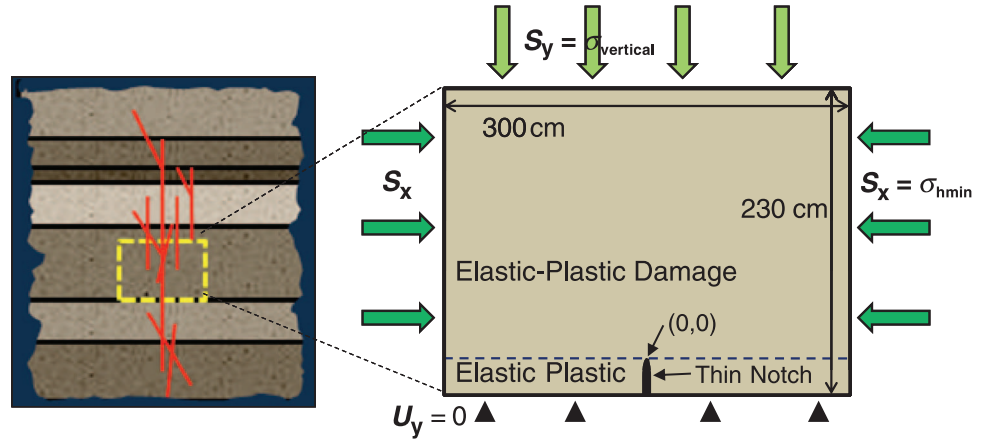
We first describe key observations of HF complexity from field and laboratory experiments. Then, the FE configuration is presented, followed by the simulation results, including (1) general morphology, (2) branching and segmentation, (3) frac-

ture arrest and rupture, and (4) loading conditions. Last, we discuss implications for fracture velocity and stability and approaches to control HF propagation.

## COMPLEX HYDRAULIC FRACTURES

Field and experimental observations reveal that simple, planar hydraulic fractures, as commonly interpreted in many reservoir applications, are relatively rare. A few examples of observed HF geometries are reviewed below. Location analysis of microseismic events during an HF operation in the Barnett Shale, Fort Worth Basin, Texas, reveals clouds of events that depend on the local stress

**Figure 2.** Geologic scenario (left) and finite element model configuration (right) for a hydraulic fracture propagating into a sandstone layer. Tectonic loads vertical stress  $\sigma_{\text{vertical}} = S_y$  and minimum horizontal stress  $\sigma_{\text{hmin}} = S_x$  are applied to the sides and internal pressure is applied in the initial vertical thin-notch fracture (see text). Displacement in the  $y$  direction is fixed at the bottom,  $U_y = 0$ .



state and proximity to folds, faults, and karst structures (Busetti and Reches, 2007; Roth and Thompson, 2009; Busetti, 2009). The fracturing mechanism of the microseismic events may also conform to the local structure. For example, high-energy microshear events induced during hydraulic fracturing were recorded in the compressive jogs of natural fracture corridors in the Carthage Cotton Valley gas field, Texas (Rutledge et al., 2004) (Figure 1D). Pre- and post-injection borehole image logs and cored intervals also suggest that, in structurally complex areas, multiple HF are likely to propagate (Warpinski et al., 1993; Fast et al., 1994; Sim, 2004).

Post-injection excavations that followed water and propping-sand treatments at depths of approximately 200 m (~656 ft) in active coal mines revealed curved and zigzag HF propagation paths, irregular aperture profiles, branching and linking segments, and terminations at layer contacts (Elder, 1977). Mapping revealed that the patterns could be linked to the dominant cleat direction or a fold axis. The influence of in-situ conditions on HF geometry was also analyzed. For example, geologic discontinuities were found to control the geometry of complex HF mapped during mineback experiments and generated in laboratory tests (Warpinski and Teufel, 1987).

Dike emplacement is a natural analog to man-made HF, and dike exposures commonly preserve the intruded, damaged host rock; the induced fracture pattern; and remnants of the injection fluid (e.g., Pollard, 1978). Arrays of en echelon dikes in sandstone, Maktesh Ramon, Israel, displayed stepped

segments and continuous linked segments (Baer and Reches, 1991). The points of intersection for the segments were located within local zones of damage composed of netlike patterns of deformation bands or in bridged zones showing evidence for pervasive shear deformation (Weinberger et al., 2000). Dike patterns near Timna Mountain, Israel, revealed subvertical contact structures and subhorizontal steps, as well as interacting segment boundaries, ridges, and grooves (Baer et al., 1994). In some locations, variations in dike thickness correlated better with the local segment attitude than with the regional setting (the overall dike length). These authors concluded that both pre-existing fracture sets and tectonic stress state controlled the dike pattern. Young clastic dikes in the Dead Sea Basin display multiple branches and segments (Figure 1C) that are likely related to an increase in inelastic energy dissipation and propagation acceleration (Levi et al., 2009).

Experimental works indicate that local stress variations may enhance, redirect, or suppress HF propagation. The stress variations may be caused by layering, preexisting discontinuities, local heterogeneity, or the presence of the HF itself. Zhou et al. (2008) conducted experiments on a fabricated sand-cement block in which they embedded planar sheets of paper at different orientations to simulate preexisting fractures. The block was loaded under polyaxial (true-triaxial) conditions, and a central borehole was pressurized by a fluid until an HF developed. The experiments showed that the applied stress state and the orientation of the pre-existing fracture control the HF propagation path

displaying three modes: HF arrest at existing fracture, crosscut of the fracture by the HF, or fracture dilating by the propagating HF.

Tortuous propagation and segmentation of the fracture front were explained by mixed-mode (I + II, or tension and shear) loading in theory (Rice, 1968) and experiments (Cooke and Pollard, 1996). Hydraulic fracturing experiments in polymethyl methacrylate (Wu, 2006) revealed that complex fracturing could be induced by injecting fluid into an initial planar circular fracture, when a small amount of torque was applied to the sample. Complex flower petal and en echelon structures with multiple twisting segments deviating up to 18° out of plane were created (Figure 1F, G) under a stress state with a shear component of only a few percent (the ratio of mode III to mode I stress intensity factors =  $K_{III}/K_I = 1-10\%$ ).

## PRESENT MODEL SETUP

### Approach

We analyze hydraulic fracture propagation in a two-dimensional (2-D) model for the following setting:

1. The host rock has a continuum elastic–plastic damage rheology that approximates the experimentally observed finite stress–strain and brittle failure of Berea Sandstone (part 1, Buseti et al., 2012).
2. Fracture propagation is determined by the local damage state of the rock and, as a consequence, failure may be simulated independently of crack-tip processes. The macroscopic failure that may occur is the process of damage fracturing developed in part 1.
3. Transient fracture propagation and the associated arrest, rupture, branching, and segmentation are investigated by the use of dynamic FE solutions.

These features can be applied with the FE code Abaqus that incorporates nonlinear constitutive behavior, finite strain, time-dependent deformation, and complex boundary conditions (part 1). For the

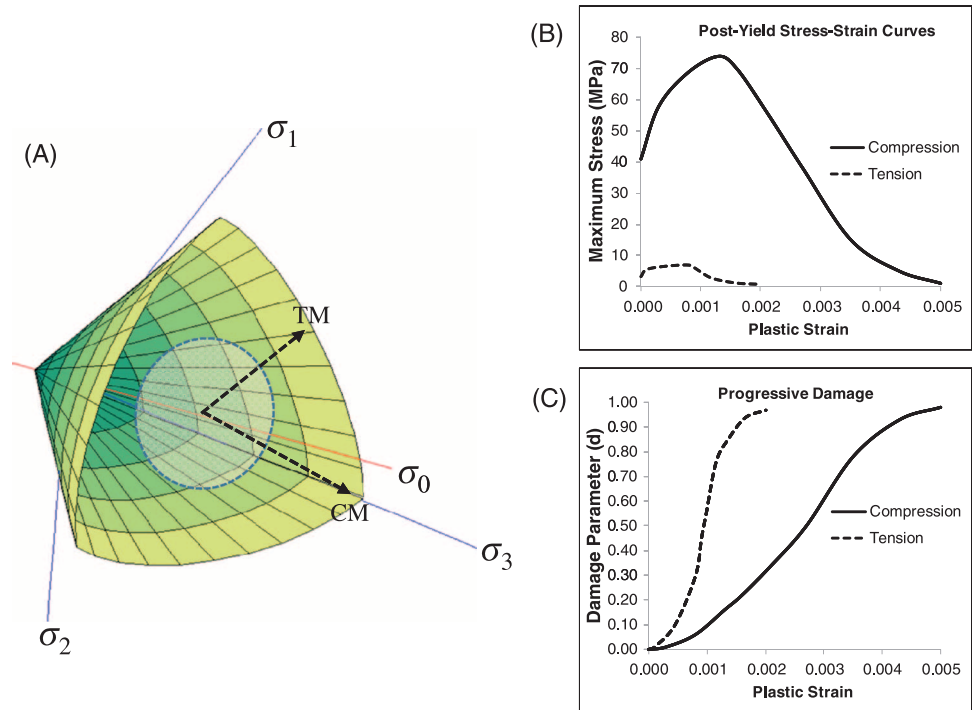
present modeling of complex fracture growth, we used the explicit solution method (Abaqus manual; Simulia, 2010a) that handles finite strain, permits simulations beyond brittle failure, and allows investigation of dynamic fracturing response. In part 1, we developed the theoretical background and calibrated the FE continuum damage rheology with rock mechanics results. These results of the damage rheology and fracture energy formulation are outlined in Appendix 1, and the explicit FE technique and the time-integration scheme are outlined in Appendix 2. The FE calculations were run using Abaqus 6.7 Extended Functionality on a Windows XP workstation with 4GB of random access memory and two 3-GHz processors working in parallel. Run times ranged from 6 to 12 hr.

## The Two-Dimensional Model

### Configuration

The model is a 2-D plane-strain, two-layer body that is 3 m (10 ft) wide and 2.3 m (7.5 ft) tall (Figure 2). The lower layer has elastic–plastic rheology, is 0.3 m (1 ft) thick, and is already fractured by a 0.3-m (1-ft)–tall vertical fracture that we refer to as the driving fracture (DF). For numerical stability, the DF is thin-notch shaped (instead of slit-like). We found a finely meshed, elliptical-tip improved resolution but it was impractical because of significantly increased run times. The DF is initially 0.5 mm at the tip and 5 mm at maximum width at the base of the model. Following tectonic loading and before pressurization, the aperture decreased to 0.2 to 0.4 mm at the tip and 1 to 4 mm at the base, depending on the horizontal stress magnitude. The upper layer has elastic–plastic damage rheology that was derived for Berea Sandstone (part 1, Buseti et al., 2012), and it is 2 m (6.6 ft) thick. The model is loaded by (1) pressurizing the DF in the lower layer that is expected to propagate upward into the upper layer, and (2) a remote (tectonic) stress of normal faulting regime ( $\sigma_v \geq \sigma_{Hmax} \geq \sigma_{hmin}$ , where  $\sigma_v$ ,  $\sigma_{Hmax}$ , and  $\sigma_{hmin}$  are the vertical, and maximum and minimum horizontal stresses, respectively.) The 2-D model represents the  $\sigma_v$ – $\sigma_{hmin}$  plane. The analyzed area is sufficiently remote from near-wellbore stress effects.

**Figure 3.** Constitutive model for the finite element (FE) damage rheology. (A) Yield surface in principal stress space and centered about the hydrostatic axis, showing tensile meridian (TM) and compressive meridian (CM). (B) Strain hardening and softening curve for tension and compression and (C) evolution of the damage parameter. The curves are based on experimental data for Berea Sandstone (part 1, Busetti et al., 2012) and are input as parameters in the FE material model.



### Constitutive Model

The upper layer has elastic–plastic damage rheology with pressure-dependent yielding, strain hardening and softening, and strain-based damage evolution in compression and tension. This rheology was derived from the concrete damage plasticity model of Abaqus that was calibrated with the experimental data for Berea Sandstone (part 1; Appendix 1). The plastic yield surface is based on the Barcelona model (Figure 3A) that is based on Mohr-Coulomb plasticity (Lubliner et al., 1989). It uses an adaptation of the Drucker-Prager cone-shaped yield surface to include the effect of the intermediate principal stress. The yield surface of this model incorporates a curved three-dimensional hexagon with tensile and compressive meridians similar to the Mohr-Coulomb model (Figure 3A). Damage and fracture propagation are simulated using the continuum damage concept. We use separate damage parameters for tension and compression that evolve independently to capture both modes I and II-III failure (Lee and Fenves, 1998). Post-failure strain softening, coupled with nonlinear damage evolution, permits extreme damage localization (Figure 3B, C). The resolution of the damage zone equivalent to a discrete fracture is determined by the coarseness of the FE mesh; an area

of damage localization is the dimension of a single element, which is 10 to 20 mm.

### Loading Procedure

We explore the propagation of the initial fracture into the overlying layer (Figure 2). Stress and injection conditions (Table 1) are selected to be loosely similar to HF operation at depths of 2011 m (6600 ft) in the Barnett Shale. The model boundary conditions are the stresses  $S_x$  and  $S_y$  on the top and sides of the model block to simulate the minimum horizontal (tectonic) and vertical stresses (overburden), respectively, and the base is locked in the  $y$  direction (Figure 2). The vertical stress is kept constant at  $S_y = 50$  MPa (7252 psi) for all simulations, and the horizontal stress ranges from  $S_x = 10$  to 45 MPa (1450–6527 psi). Pressure ( $P_f$ ) is applied inside the existing fracture in the lower layer to simulate fluid injection. In the model,  $S_x$  and  $S_y$  and gravity are loaded first, followed by two steps of pressurizing the fracture in the lower layer. First, the DF pressure,  $P_f$ , is instantaneously increased from 0 to  $S_x + 5$  MPa (725 psi), which is below the layer breakdown pressure. Then, ( $P_f$ ) is incrementally increased until either total failure of the layer occurs or the solution becomes unstable.

**Table 1.** Summary of Simulations

Test	Load Configuration			Damage Distribution			
	Tectonic State of Stress (Mpa)		Rate of Extension (mm/s)* $d_x/2$	Internal Pressure Distribution	Pattern of Main Fracture Path ( $d > 0.5$ ) <sup>†</sup>	Pattern of Damage ( $0.01 < d < 0.1$ ) <sup>††</sup>	Shape ( $l/w$ ratio)** ( $d = 0.01$ )
	$S_x$	$S_y$					
1	10.0	50	N/A	Uniform	Complex, long	Pervasive, bifurcated	0.8–1.2
2	12.5	50	N/A	Uniform	Complex, long	Pervasive, bifurcated	0.7–1.4
3	15.0	50	N/A	Uniform	Complex, long	Pervasive	0.8–2.0
4	17.5	50	N/A	Uniform	Complex, long	Pervasive, bifurcated	0.7–1.5
5	20.0	50	N/A	Uniform	Complex, short	Pervasive, asymmetric	0.6–1.7
6	22.5	50	N/A	Uniform	Complex, short	Pervasive, symmetric	0.5–1.6
7	25.0	50	N/A	Uniform	Long, straight	Teardrop tip	2.2
8	30.0	50	N/A	Uniform	Long, straight	Small teardrop tip	3.1
9	35.0	50	N/A	Uniform	Long, straight	Small teardrop tip	4.2
10	40.0	50	N/A	Uniform	Simple short branches	Asymmetric bridging	2.6
11	45.0	50	N/A	Uniform	Complex, short	Pervasive, irregular	0.3–0.4
12	10.0	50	N/A	Nonlinear	Complex, long	Pervasive, bifurcated	0.9–1.3
13	12.5	50	N/A	Nonlinear	Complex, long	Pervasive, bifurcated	0.6–1.2
14	15.0	50	N/A	Nonlinear	Complex, long	Pervasive, bifurcated	0.6–1.2
15	17.5	50	N/A	Nonlinear	Complex, long	Pervasive, bridging	1.4
16	20.0	50	N/A	Nonlinear	Complex, long	Asymmetric bridging	2.1
17	22.5	50	N/A	Nonlinear	Long linking segments	Symmetric bridging	N/A
18	25.0	50	N/A	Nonlinear	Long linking segments	Symmetric bridging	1.8
19	30.0	50	N/A	Nonlinear	Long, straight	Teardrop tip	2.8
20	35.0	50	N/A	Nonlinear	Long, straight	Teardrop tip	3.1
21	40.0	50	N/A	Nonlinear	Simple short branches	Asymmetric bridging	2.6
22	45.0	50	N/A	Nonlinear	Complex, short	Pervasive, lateral	0.5

\*N/A = not applicable.

\*\* $l/w$  ratio = length-to-width ratio of damage pattern measured in the  $y$  and  $x$  directions for a minimum  $d$  of 0.01.

<sup>†</sup>Main fracture path interpreted as elements having a damage ( $d$ ) value greater than 0.5.

<sup>††</sup>Limits of damage  $d$  in contour plots used to interpret the observed patterns.

The  $P_f$  increases at a constant rate of 10 MPa/s (1450 psi/s), which is approximately ten times faster than is experienced during typical pumping, but leads to more efficient solution times.

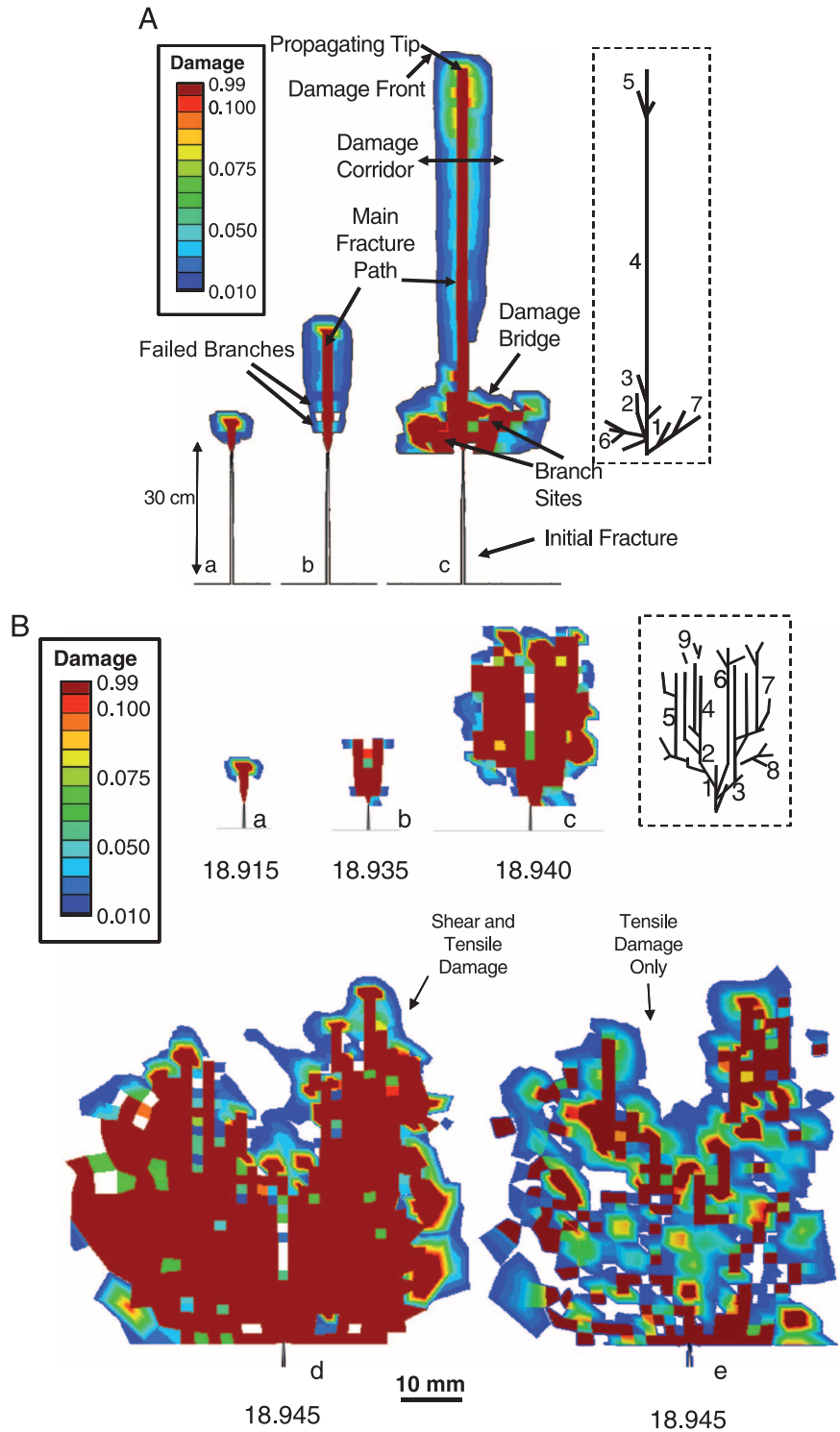
The models simulate dry propagation, with fracture pressurizing based on fluid lag conditions (e.g., Figure 1E). No fluid penetrates through the fracture walls, into the fracture-tip region, or ahead of the fracture into the newly formed fractures. These conditions of a local impermeable zone of microcracking ahead of the fracture and the advancing fluid front subsequently penetrating into the dry fracture tip are consistent, for example, with fracturing very tight rocks or while using highly viscous fluids (e.g., Van Dam et al., 1999).

The latter case affects the pressure distribution in the fracture, which depends on the viscosity and type of injection fluid, for example, oil versus water in the experiments of Ishida et al. (2004). We thus consider two cases: one of uniform pressure (water) and one of highly viscous fluid. We used the following equation to calculate the nonlinear pressure distribution within a fracture pressurized by a viscous fluid (from Ishida et al., 2004):

$$d_p/d_L = 12\mu q/w^3 \quad (1)$$

where  $d_p/d_L$  is the pressure drop along the fracture length,  $L$ ,  $\mu$  is the viscosity,  $q$  is the flow rate, and  $w$  is the maximum aperture.

**Figure 4.** (A) Time-sequence damage contour plots showing the main features of damage fracturing. The load case shown is for no internal fracture pressure and a constant lateral strain rate of  $16.7 \times 10^{-5}$  is applied to the sides of the model. The color scale reflects the intensity of damage by microcracking simulated at three time intervals. The scalar stiffness degradation variable (SDEG) (both tension and compression damage) is plotted. The dark red area is interpreted as the main fracture path, where damage has completely localized and zero stiffness is observed. An interpreted fracture map for c is shown at the right side where numbers indicate branching level. (Note that, because damage variables are isotropic in the current formulation, interpreting fracture growth direction is only possible by observing linkage between elements. An anisotropic damage tensor is needed to quantitatively interpret discrete fracture propagation direction within each element.) (B) Time-sequence damage contour plots showing evolution of the main morphological features for a hydraulic fracture propagating under very high differential stress tectonic regime ( $S_x = 10$  MPa [1450 psi],  $S_y = 50$  MPa [7252 psi]; test 1, see Table 1). Numbers shown next to each frame are the corresponding internal fracture pressure in megapascals. Frame e shows a plot of the final stage in d, but only showing tensile mode of damage,  $d_t$ . An interpreted fracture map for c is shown at the right side where numbers indicate branching level. (C) Time-sequence damage contour plots showing evolution of the main morphological features for a hydraulic fracture propagating under moderate differential stress tectonic regime ( $S_x = 25$  MPa [3626 psi],  $S_y = 50$  MPa [7252 psi]; test 7, see Table 1). Numbers shown next to each frame are the corresponding internal fracture pressure in megapascals. Frame f shows a plot of the final stage in e, but only showing tensile mode of damage,  $d_t$ . An interpreted fracture map for e is shown at the right side where numbers indicate branching level.



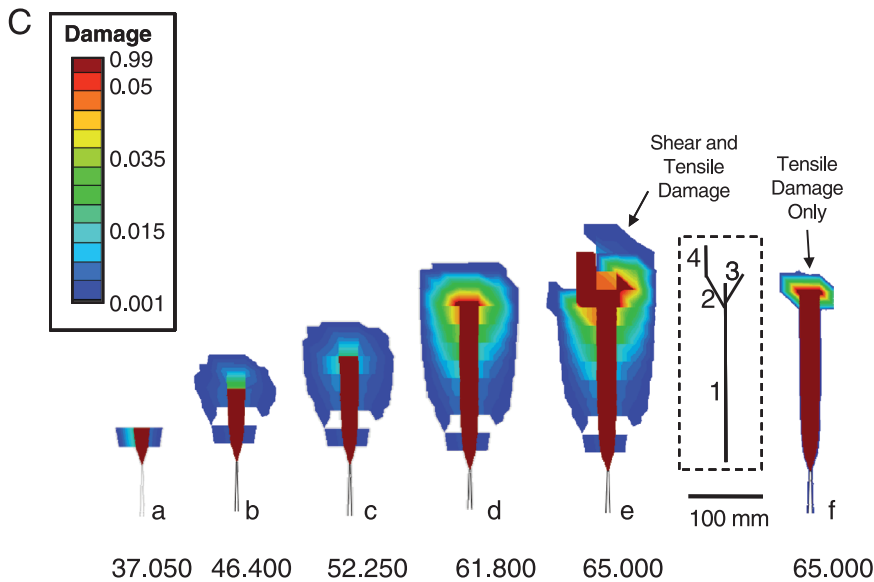


Figure 4. Continued.

## RESULTS

### General

A total of 22 HF simulations were completed, 11 each for the uniform and nonuniform pressure distribution in the lower layer fracture (Table 1). Moreover, to compare the results with a simpler configuration of pure extension, several simulations were run with no internal pressure and loading was applied by extending the sides at a constant strain rate (Figure 4A). The simulation results are discussed in the following topics:

1. Fracture morphology: damage corridor, segments, and branches
2. Fracture dynamics: fracture arrest, rupture patterns, and stress path

Note the following three points while inspecting the results. First, the elastic–plastic damage rheology of the model has no time-dependent components (e.g., viscous effects). Thus, observed strain-rate dependency is solely related to the kinetic effect (inertial effects) of loading and failure and not to the rheologic definition. Second, the subsequent discussion and figures quantify the amount of damage using the damage parameter,  $d$ . Unless otherwise specified (e.g.,  $e$  in Figure 4B,  $f$

in 4C),  $d$  reflects the combined damage from tension and compression (Abaqus field output SDEG, the scalar stiffness degradation variable) and is equal to the local stiffness degradation; for example,  $d = 0.9$  means that 90% of the original stiffness has been lost. The parameter  $d = 0$  is for undamaged rock;  $d \sim 0.4$  coincides with the ultimate stress limit and is generally assumed to be related to widespread damage (e.g., Lyakhovsky et al., 1997; Chen et al., 2006); and  $d = 1$  represents a pervasively damaged, completely failed region with stiffness equal to zero. Third, during the propagation periods of the simulations, field output data (e.g., stress and strain) were recorded at 0.001-s intervals, and energy variables (entire system) were recorded at 200 equal intervals.

### Fracture Morphology

#### The Damage Corridor

The main features that are common to most simulations are presented by snapshots of the simulations without fracture pressurization (tectonic extension only) and are shown in Figure 4A. Runs with fracture pressurization are shown in Figures 4B and C and 5. At the onset of dilation, two symmetric, least compressive stress lobes form at the tip of the initial fracture (not shown). With continued

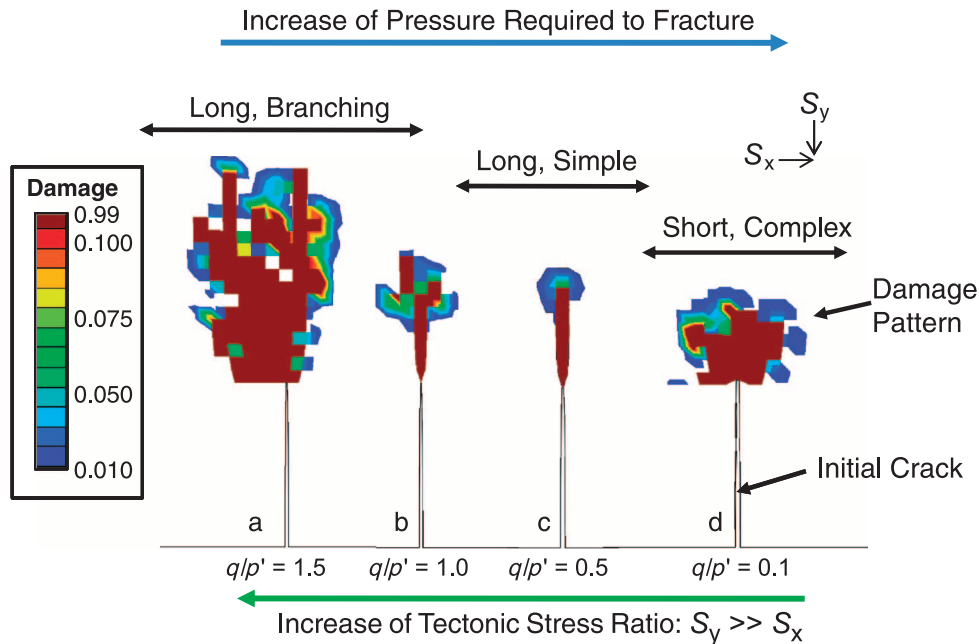


**Figure 5.** Hydraulic fractures formed under a range of stress regimes (a corresponds to test 2 from Table 1; b = test 5; c = test 8; d = test 11). Results are shown as a function of tectonic stress ratio according to the  $q/p'$  convention, where  $q$  and  $p'$  are the deviatoric and pressure stress for plane strain. The length of the initial fracture (black outline) is 30 cm (12 in.). The outer patterns (strongly heterogeneous or strongly homogeneous) show complex segments with no distinct main fracture path and display multiple branches and linking segments, and the overall damage distribution is pervasive. The inner patterns (weakly heterogeneous) are simple segments with narrow symmetric zones of damage that extend uniformly over time.  $S_x$  is the minimum horizontal stress.  $S_y$  is the vertical stress.

dilation, the lobes become increasingly more tensile, and their size gradually widens ahead of the fracture. When the plastic yield limit is reached, quasisymmetric lobes of damage up to 100 mm wide begin to form within the tensile region ahead of the fracture tip (Figure 4A). This broad, weak damage front ( $d < 0.1$ ; Figure 4A) is followed by a propagating fracture tip that migrates upward with continued extension and leaves behind a damaged zone, which is defined here as the damage corridor. The damage corridor (Figure 4A) is loosely related to the shielding zone (Thompson, 1986) or the process zone (Reches and Lockner, 1994). However, unlike the last two that are restricted to the tip of the fracture, the damage corridor may grow far ahead of the initial fracture and be much longer than the initial fracture (Figure 4B). The damage intensifies and localizes within a narrow zone approximately 10 to 20 mm wide (one element width) in the center of the damage corridor (Figure 4B) with  $d$  of approximately 0.99 that corresponds to a completely failed fracture zone. The damage

corridor continues to grow in a series of buildup and release cycles that are discussed below.

### Branching and Segmentation

Prolonged lateral damage intensification without upward propagation results in the formation of multiple potential sites for branching (e.g., b in Figure 4A, B; a in Figure 4C). We envision that, later, when the pressurized fluid propagates into the damage corridor (a process not simulated here), these potential branch sites could become active growing branches or remain as a fracture-wall damage. Active branches grow in length and may eventually coalesce with the main path (e.g., late stages in Figure 4B). Failed branches (e.g., b in Figure 4A, B; a in Figure 4C) are lobes of damage extending obliquely from the main fracture path that do not grow significantly in length. They are damage sites where fracture-wall leak-off may occur. The overlapping of closely spaced failed branches creates the net effect of an intensified damage corridor, where  $d = 0.01$  to 0.05. Fracture

segments are disconnected branches that form out of sequence from the main fracture path and may be isolated, connected by bridges of damage, or are fully linked to the main fracture (e.g., a in Figure 5).

Branches and segments develop through complex transient propagation stages that depend on the load configuration. For example, during the pressurization simulations, the branches and segments become more dominant in states of reduced differential stress (d in Figure 5). However, a moderate differential stress produces simple fractures (c in Figure 5), characterized by in-plane growth, where damage evolution is similar in early and late stages of growth. Very high (Figure 4B, a in Figure 5) or very low differential stress (d in Figure 5) produced complex fracture networks.

The order of damage evolution also varies. For the simple patterns (e.g., c in Figure 5), regions of rock in the main damage path initiate and evolve in sequence, and the timing between rupture events is uniform; the fracture grows continuously by uniform rupture and arrest events. For the complex case (Figure 4B), damage develops out of sequence and multiple segments initiate and grow contemporaneously. This out-of-sequence growth has an adverse effect on local stability by creating weakened patches of rock, that is, generating flaws, ahead of the crack tip. Such growth reflects discontinuous fracture development by damage bridging and fracture linkage (e.g., c in Figure 4A, B), a process that might also be expected in mechanically heterogeneous rock, for instance, in naturally fractured rock layers.

## Fracture Dynamics

### Arrest and Ruptures

Our FE simulations provide a powerful tool to recognize nonsteady fracture growth. In the simulations, the fluid pressure in the initial fracture (Figure 2),  $P_f$ , was increased at a constant rate of 10 MPa/s (1450 psi/s). The high recording rate (1 kHz) allows detailed identification of nonuniform fracture growth rate. We interpret this nonuniform growth rate as intrinsic behavior of local stress buildup and release, which we correlate to rupture and arrest features observed on

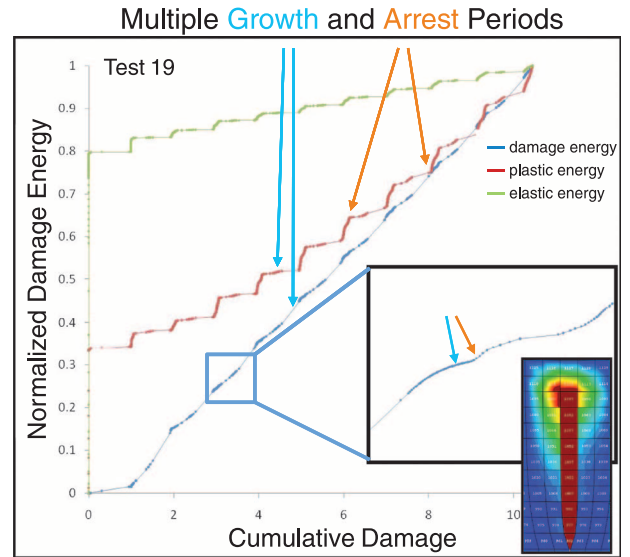
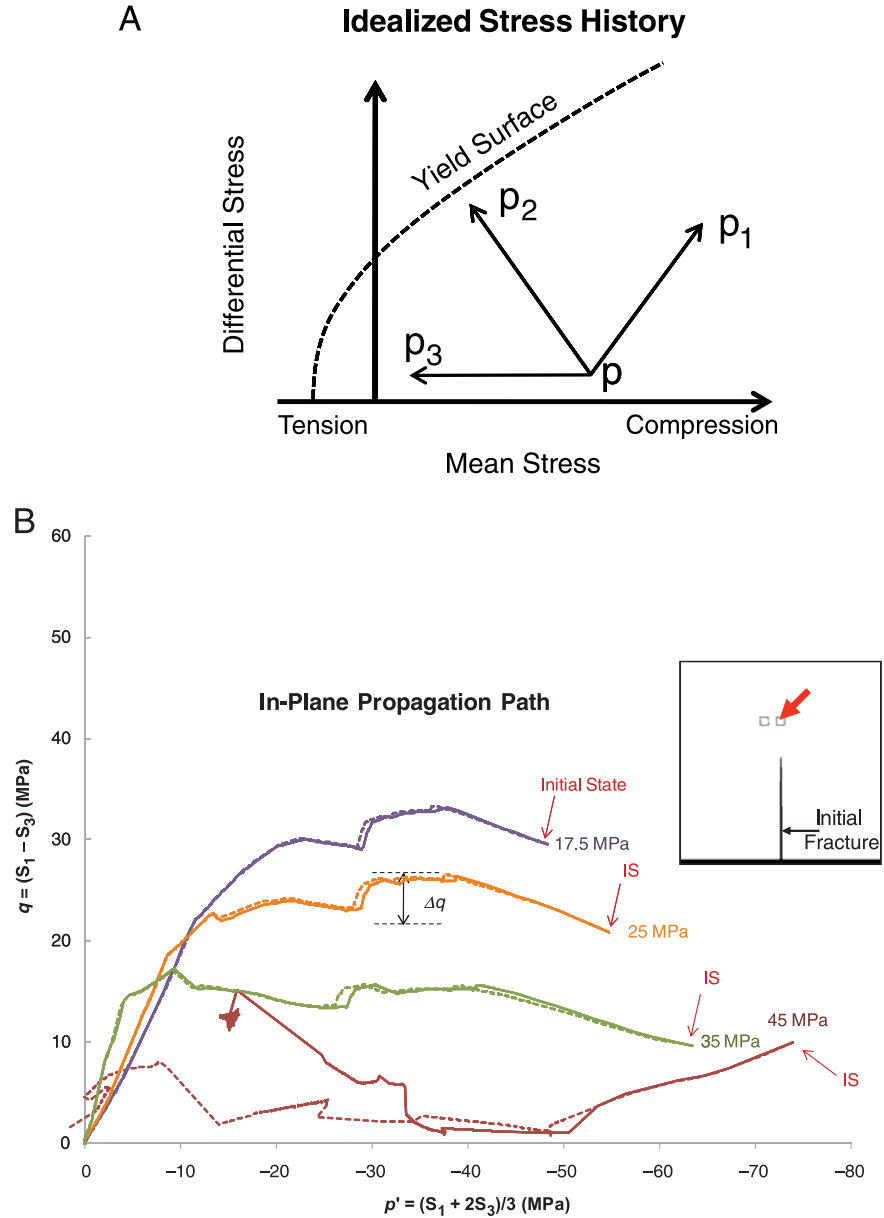


**Figure 6.** Evolution of cumulative damage ( $x$  axis) versus normalized dissipated damage energy ( $y$  axis), the ratio of the cumulative damage energy at a current increment to the total damage energy at the last measured increment, for test 19 (see Table 1). Each line represents an element in the main fracture path. The steeper the slope, the more unstable the propagation. The small dots reflect equal 0.001-s time intervals. Closely spaced dots indicate slow propagation, whereas widely spaced dots are periods of fast propagation. Cumulative (global) pattern shows a stair-stepping pattern indicating buildup and release periods, reflective of stable or unstable fracture growth and related to local dynamic behavior. The lines are for elastic (green), plastic (red), and damage (blue) dissipated energy. The inset is a close-up image of rupture-arrest period. The inset on the right side is a contour map of the damage pattern.

tensile joints (e.g., Cosgrove and Engelder, 2001) and dikes (Baer et al., 1994). During buildup stages, the damage corridor widens and intensifies (e.g., lower failed branches in b in Figure 4A), whereas during release stages, the damage corridor (and main fracture path) extends in length (e.g., upper main fracture path in b in Figure 4A). The growth cycle starts with a rupture and concludes with an arrest as demonstrated in Figure 6.

The arrest and rupture sequence is presented for a relatively simple fracture in the case  $S_x = 25$  MPa (3626 psi) (Figure 4C). At the initial fracture tip, a leftward asymmetric damage cloud develops continuously beginning under  $P_f = 35.75$  MPa (5185.10 psi). Then, until  $P_f = 37.05$  MPa (5373.65 psi), damage begins to develop on the right side, resulting in a 65-mm-wide by 46-mm-long T-shaped main fracture path (a in Figure 4C).

**Figure 7.** (A) Yield surface and idealized stress paths for tectonic loading ( $p_1$ ), a normal faulting state of stress ( $p_2$ ), and an increasing internal fracture pressure ( $p_3$ ). (B) Stress path for a region in-plane to the main fracture path (inset, red arrow), plotted for four tectonic stress states (labeled by the  $S_x$  value).  $S_1 = S_y$  is the maximum principal stress;  $S_3 = S_x$  is the minimum principal stress. Differential stress  $q = (S_1 - S_3)$ . Mean stress  $p' = (S_1 + 2S_3)/3$ . Solid lines are for tests with a uniform pressure distribution, whereas dashed lines are for those with nonlinear distribution. The initial state (IS) of stress for the region is at the far right side of the curves. With internal pressurization and as damage advances, the local stress changes for the region and the stress path follows the curve to the left. Failure occurs when the path intersects the yield surface (not plotted). (C) Stress path for a region off-plane to the main fracture path (inset, orange arrow), plotted for four tectonic stress states.



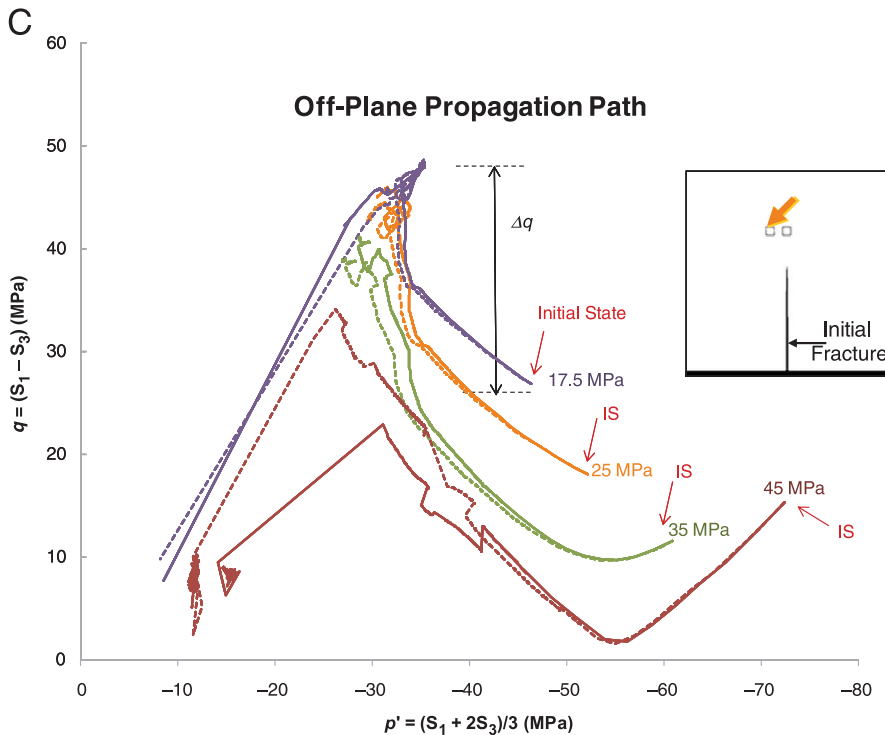
The fracture does not propagate further until  $P_f$  increases to 38.45 MPa (5576.70 psi); this is the stress buildup period that we refer to as an arrest stage. Then, the main fracture extends vertically from the center intersection point in a rupture stage and grows to approximately 30 mm. In a series of ruptures, the main fracture path grows and damage bridges linking the left and right branches form to create a slightly asymmetric 118-mm-wide by 92-mm-long complex damage corridor (b in Figure 4C). Subsequent failed branches form with decreasing spacing (c in Figure 4C), leading to a roughly symmetric, elongated teardrop-shaped

damage zone that encloses the straight, main fracture path (d in Figure 4C). At  $P_f = 65$  MPa (9427 psi) (e in Figure 4C), the main fracture length is approximately 230 mm; at the damage front, two branches that form vertical 69-mm-long left- and 46-mm-long right-stepping segments are observed.

**Stress Path Analysis**

The FE simulations provide a detailed stress history (stress path) for each element. We plot (Figure 7) the stress paths for four load configurations ( $S_x = 17.5, 25, 35, 45$  MPa [2538.2, 3626, 5076, 6527 psi])

Figure 7. Continued.



and for two elements located differently with respect to the initial pressurized fracture. The in-plane element is located exactly above the fracture tip at  $x = 0$  and  $y = 100$  mm (red arrow, Figure 7B), and the off-plane element is located slightly off the vertical continuation of the fracture at  $x = -50$  mm and  $y = 100$  mm (orange arrow, Figure 7C). The in-plane element is likely to reflect the stress path in the center of the damage corridor in contrast to the off-plane element.

The initial stress state (far right side of Figure 7B, C) reflects the end of the tectonic loading stage ( $S_x$  and  $S_y$  applied). The stress path from DF pressurization,  $P_f$ , advances to the left with pressure (or time). Upon intersection with the yield envelope (not plotted) of the element, the path either moves downward along the yield surface according to the plasticity rule or fluctuates depending on the variations of the local stresses. Idealized stress paths are depicted in Figure 7A to demonstrate the stress history at a point of rock subjected to increased tectonic loading ( $p_1$ ), relaxation of horizontal stresses as in a normal faulting environment ( $p_2$ ), and increasing fracture internal pressure (or pore pressure) under constant tectonic stress ( $p_3$ ).

The simulated stress-path plots display the overall effects of load conditions on hydraulic fracturing as follows (reference to locations in Figure 7B, C):

1. Tectonic conditions determine the general propensity to fracture. The local stress state establishes how close the material at a given location is to the yield surface. Under high differential stress, the rock is already close to failure and requires only small additional fracture pressurization. However, a low differential stress state requires significant pressurization to approach failure. Note that the stress field is not uniform because of local amplification, for example, because of the fracture tip. For instance, in the case of  $S_x = 45$  MPa (6527 psi) (red curve in Figure 7B, C), the in-plane element stresses (Figure 7B) are  $p' = 73.9$  MPa (10,718.3 psi) and  $q = 10$  MPa (1450 psi), where  $q$  is the deviatoric stress and  $p'$  is the pressure stress (equation 2a and b), whereas the off-plane element stresses (Figure 7C) are  $p' = 72.5$  MPa (10,515.2 psi) and  $q = 15.3$  MPa (2219.1 psi).
2. Stress evolution is controlled by the increasing DF pressure. The stress path at each location of

rock conforms to a family of curves that steepens for states of high differential stress (e.g.,  $S_x = 17.5\text{-MPa}$  [2538.2-psi] curve, Figure 7B) and inverts for very low differential stress states (e.g.,  $S_x = 45\text{-MPa}$  [6527-psi] curve, Figure 7B). For the off-plane element (Figure 7C), the average prefailure change in  $q$  is 20 to 30 MPa (2901–4351 psi), whereas for the in-plane element (Figure 7B),  $q$  ranges from only 3 to 5 MPa (435–725 psi). Low differential stress states at high mean stress are not optimal for tensile fracturing and the stress path takes a long indirect route to intersect the yield surface. This result suggests that the common practice of treating pore pressure and fracture pressure equally in an effective stress framework (e.g., pressurization equals a leftward shift of the Mohr circle) is only a global approximation of the stress path and may not represent the actual local failure mode.

3. Regions within the in-plane zone predominantly fail because of reduction of the hydrostatic pressure. On a Mohr diagram (Figure 7A), this is approximated as a circle of nearly constant diameter moving to the left until intersecting the failure envelope, an effect common during elevated pore pressure. However, per Point 2, this does not necessarily indicate tensile failure, as the shear contribution (change in  $q$  stress) also depends on the evolving local stress state.
4. Regions within the off-plane zone (away from the main fracture path), but still within its area of influence, fail via increased differential stress and pressure reduction. This is reflected on a Mohr diagram (Figure 7A) as a circle that intersects the failure envelope by both size increase and shift toward low normal stress. This path is consistent with normal faulting conditions and explains the proclivity for microseismic shear events associated with DF propagation. Furthermore, it readily can be deduced that, if the DF encounters natural fractures or faults, such that the rock rheology is anisotropically damaged (i.e., for a given orientation, the yield surface is essentially cohesionless and the internal angle of friction is replaced by the lower value for contact or sliding friction),

the tendency for shear failure may be further enhanced.

5. The effect caused by changing the DF pressure distribution decreases with tectonic stress ratio and increases adjacent to the main fracture path. For a nearly homogenous stress state and a uniform pressure distribution, the stress path for the in-plane region of rock shifts to become influenced more by the differential stress (solid red line bends upward to the left in Figure 7B). Moreover, for these conditions, the stress paths for in-plane (solid red line, Figure 7B) and off-plane propagation (solid red line, Figure 7C) are quite similar. This suggests that, in very weakly tectonically stressed areas, mixed-mode fracturing is most likely to happen unless very viscous fluids are used.

## DISCUSSION

### Loading Control of Fracture Propagation

We mapped the damage of the models as a function of hydraulic fracture pressure and tectonic stress for all runs: simulations with uniform DF pressure are shown in Figures 8 and 9A, and simulations with a nonuniform pressure are shown in Figure 9B. Cumulative damage is plotted as a function of fluid pressure and tectonic stress, according to the  $q/p'$  convention, where  $q$  and  $p'$  are the deviatoric and pressure stresses, respectively, for plane strain. Thus,

$$\text{Net } P/q = (P - S_3)/(S_1 - S_3) \quad (2a)$$

(normalized fluid pressure)

$$q/p' = (S_1 - S_3)/([S_1 + 2S_3]/3) \quad (2b)$$

(normalized tectonic stress)

where  $P = P_f$  is the DF pressure for the DF in the lower layer (Figure 2);  $S_1 = S_y$  is the maximum principal stress;  $S_3 = S_x$  is the minimum principal stress; and  $(P - S_3)$  is the effective fracture pressure. The amount of damage is quantified by the sum of all damage accumulated in the entire upper layer. Figure 8 displays the cumulative sum of tension and shear damage,  $d_{\text{tot}} = \Sigma(d_c + d_s)$  and Figure 9

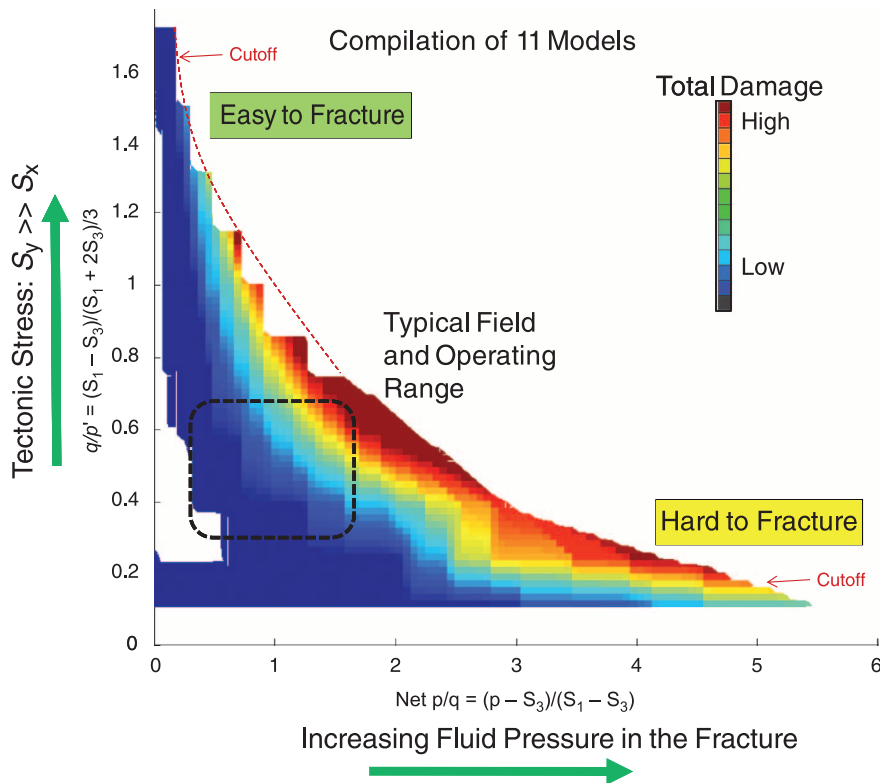


**Figure 8.** Contour map showing cumulative damage evolution versus fluid pressure ( $x$  axis) and tectonic stress state ( $y$  axis). Results are shown as a function of tectonic stress ratio according to the ratio of  $q/p'$  where  $q$  and  $p'$  are the deviatoric stress and pressure stress, respectively, for plane strain. Net  $P$  is the effective fracture pressure ( $P - S_3$ ),  $P$  is the fluid pressure in the driving fracture,  $S_1 = S_y$  is the maximum principal stress, and  $S_3 = S_x$  is the minimum principal stress. Warm colors indicate high damage and also suggest greater fracture connectivity (see text). The curved boundary on the right side reflects the pressure needed to induce total failure of the layer. Layers under high tectonic stress are easy to fracture but create little damage. In areas of low tectonic stress, a lot of damage develops, but high fluid pressure is required to initiate fracturing. The dashed black box reflects typical reservoir conditions.

displays the cumulative ratio of shear to tensile damage, wherein the ratio =  $\Sigma d_s / \Sigma d_t$ . The two plots are discussed below. In the previous section, we used cumulative damage to explain the process of damage evolution, and here, we apply the cumulative damage to serve as a proxy for fracture connectivity. In the FE scheme, damage is distributed by elements, and the elements are capped at a value of  $d = 1$ . For example,  $d_{tot} = 10$  reflects the equivalent of 10 completely damaged elements, here equal to approximately  $0.005 \text{ m}^2$  ( $\sim 0.054 \text{ ft}^2$ ). Small elemental damage values that indicate the onset of microcracking but do not imply macro-scale connectivity do not significantly contribute to the cumulative damage.

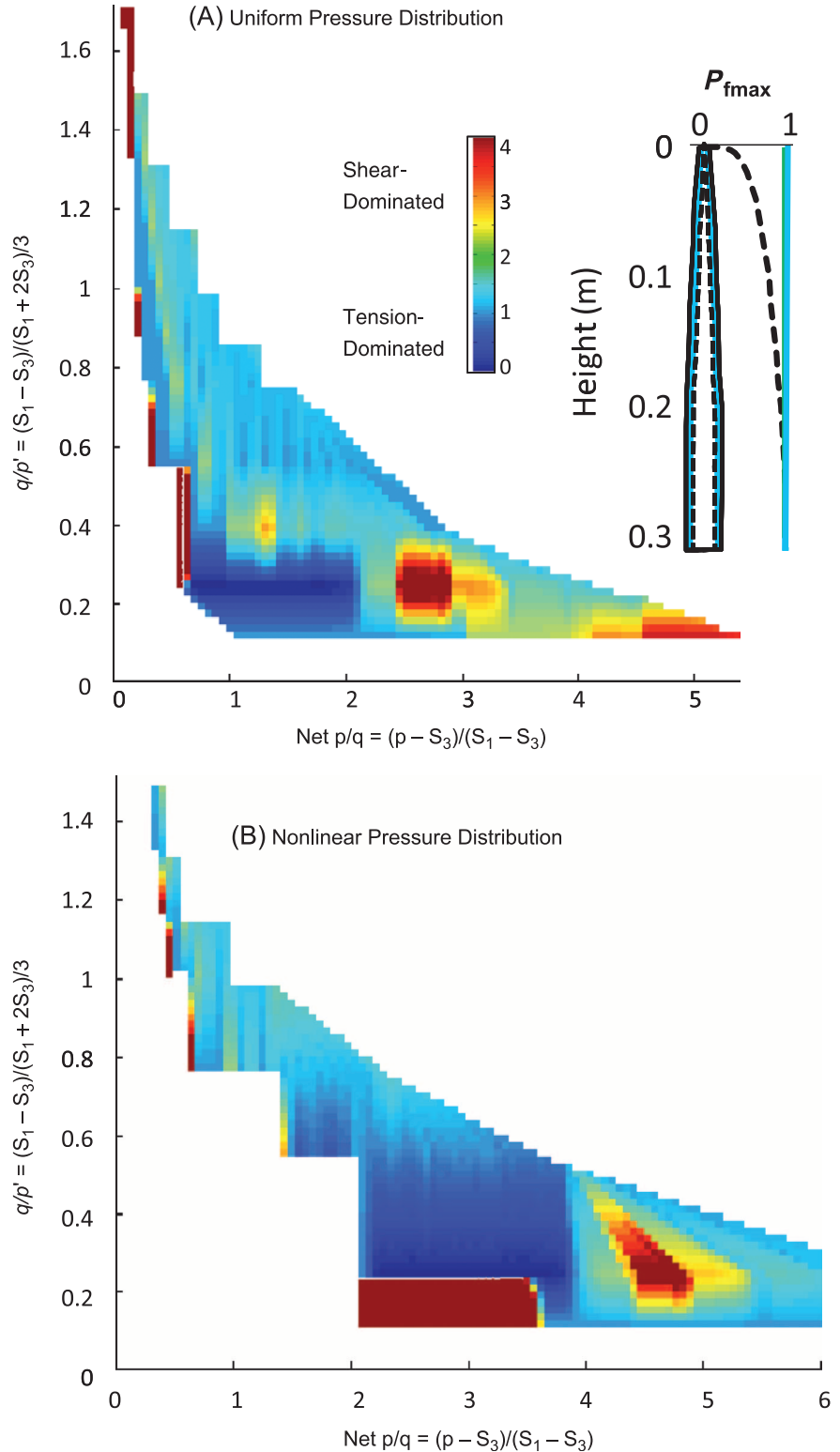
### Tectonic Load and Fluid Pressure

Figure 8 displays the results of 11 simulations with a uniform pressure in the DF. The black dashed box marks the range of tectonic stresses for a typical field and injection pressures for normal operating conditions based on data from approximately one dozen wells in the Barnett Shale, Texas. The curved boundary, marked as cutoff, which extends

from the top left side to bottom right side is the damage boundary, a value of  $d_{tot} = 12$  that corresponds to total failure of the upper layer.

Figure 8 displays the competition between two partly independent processes: distributed damage with high fracture connectivity, which is shown by the color grading, and total failure of the layer by simple fractures with low connectivity, which is marked by the cutoff line. Simulations with high tectonic stress ratio ( $q/p' > \sim 1.0$ ) require low injection pressure to induce complete failure of the layer (net  $P/q < 1$ ) and can be thought of as easy to fracture. However, these simulations accumulate little damage before layer failure and thus suggest limited fracture connectivity apart from the main fracture path. Simulations with tectonic stress ratios more than approximately 0.8 indicate layer failure under relatively low  $P_f$  (net  $P/q \sim 1$ ). Simulations with tectonic stress ratios between approximately 0.2 and 0.8 could run to total failure only under very high injection pressure (net  $P/q > 2$ ). Furthermore, at the lowest tectonic stress ratios ( $q/p' < \sim 0.2$ ), pressures in the cutoff area led to failure of the DF wall and shear failure at the

**Figure 9.** Contour plots of the ratio of damage in compression to damage in tension for all 22 hydraulic fracture simulations. Results are shown as a function of tectonic stress ratio according to the  $q/p'$  convention, where  $q$  and  $p'$  are the deviatoric stress and pressure stress, respectively, for plane strain. Net  $P$  is the effective fracture pressure ( $P - S_3$ ),  $P = Pf_{\max}$  is the fluid pressure in the driving fracture,  $S_1 = S_y$  is the maximum principal stress, and  $S_3 = S_x$  is the minimum principal stress. The scale bar is suppressed for clarity: vertical axis is  $q/p' = 0$  to 1.7 in A and 0 to 1.5 in B; horizontal axis is net  $P/q = 0$  to 5.5 in A and 0 to 6 in B. The two pressure distributions and fracture profiles are shown in the upper right side of the inset. Warm colors indicate a shear-dominated failure and cool colors indicate tensile failure. For the uniform pressure distribution (A), failure has both shear and tensile components. For the nonlinearly distributed pressure tests (B), the tensile component dominates. Moreover, in B, the pressure required to induce damage and total layer failure is higher than that in A.



layer boundary. However, these simulations with tectonic stress of 0.2 to 0.8 that are hard to fracture generate intense damage suggesting high fracture connectivity.

### Effects of Fracture Pressure Distribution

The pressure distribution in the DF, which depends on the injection fluid properties, affects the HF development (e.g., Ishida et al., 2004). As

in equation 1, the pressure drop associated with water or light-sand injection is much less than if the fluid contains coarse sand proppant or gel, or as in the extreme case, is magma. The idealized uniform pressure condition introduces a shear component at the fracture tip, which, when accommodated inelastically, deviates from mode I behavior. The experiments of Wu (2006) demonstrated that just a few percent of shear component led to complex fracturing. In the experiments of Ishida et al. (2004), HFs generated from injecting viscous oils created planar cracks with few branches, whereas water generated wavelike fractures with many branches.

We used uniform pressure to approximate water injection and nonuniform pressure (equation 1) for a viscous fluid. Simulations with a uniform pressure distribution produced an elliptical fracture profile with a relatively blunt fracture tip, whereas simulations with nonuniform pressure distribution produced fractures with a cusped shape and a relatively sharp tip (upper right side, Figure 9). The damage process was affected as the fracture profile and fracture-tip geometry changed. The onset of damage and the total layer failure for the nonuniform pressure distribution (Figure 9B) occur at a higher injection pressure than for the uniform case (Figure 9A), indicating that it is easier to induce and propagate fractures under a uniform pressure distribution. The effect becomes more pronounced as the tectonic stress ratio decreases.

The main distinction between the simulated damage patterns for the two distributions is in the relative intensity of tensile damage versus shear damage (Figure 9). Microstructural mapping (Katz and Reches, 2004; Backers et al., 2005) and focal mechanism analyses (Chang and Lee, 2004; Ishida et al., 2004; Backers et al., 2005) indicate that both shear and tensile microcracking occur during fracture propagation and the results of Ishida et al. (2004) indicated that shear mechanisms dominated the formation of the complex fractures.

The quantification of shear and tensile events is not simple. Laboratory and field detection techniques, such as acoustic emissions and microseismicity, are likely to undersample the tensile events that have relatively lower energy (e.g., Sasaki, 1998),

and in general, shear microcracks are commonly not anticipated because the fracture toughness of mode I fractures is smaller than the fracture toughness of mode II fractures ( $K_{IC} < K_{IIC}$ ) (Katz and Reches, 2004). However, in our FE simulations, we could clearly distinguish between the tensile and shear failures that we present in Figure 9 by the ratio of shear damage ( $D_c$ ) to tensile damage ( $D_t$ ). Under moderate differential tectonic stress ( $0.4 > q/p' > 0.8$ ) (Figure 9A, also see Figure 7), the uniform pressure produces a higher proportion of  $D_c:D_t$  (Figure 9A), whereas the damage in the nonuniform distribution is more tensile (Figure 9B). A uniform pressure slightly decreases the frequency and increases the intensity of the buildup stages (e.g., Figure 6) that are responsible for the development of off-plane segments and branches.

It was shown that permeability increases appreciably during tensile microcracking dilation and, to a lesser extent, during shear dilation (e.g., Zoback and Byerlee, 1975; Ostensen, 1983; Zhu and Wong, 1999; Simpson et al., 2001). We expect that fluid penetration into and reactivation of even weakly developed failed branches would create the additional complexity of pressure heterogeneity that could further contribute to complex damage propagation. Additionally, damage accumulation along the fracture wall will increase the leak-off rate and could have additional implications on proppant embedment.

## Implications for Fracture Velocity and Stability

The dynamic interchange between stages of buildup and rupture reflects the transitions of the rock through various deformation stages (i.e., elasticity, strain hardening, yielding, and strain softening) (Figure 7). In addition to loading conditions, the constitutive behavior dictates how energy builds up and releases. In the present rheologic model, the material is defined to be rate-independent and viscous effects are ignored; however, as we now discuss, the time-sequence and kinetic effects associated with damage dissipation affect fracture development. The damage evolution for the material, which reflects the dissipated fracture energy, equals the area under the load-displacement curve. When

the work applied to the system is accommodated elastically, no damage accumulates and no energy is dissipated by microfracturing. We envision that the pressure increase in the DF first increases the elastic stress that then activates the microcracking damage (if the location is above the yield point). If the rate of energy dissipated by microcracking (blue line in Figure 6) is equal or less than the rate of elastic stress buildup (green line in Figure 6), the ruptures will be stable. However, if the elastic energy builds up faster than microcracking dissipation, the ruptures will be unstable and will generate more damage (e.g., Figure 4B).

Velocity and inertial effects contribute to the release of stored kinetic energy during yielding. Figure 6 displays an example of this damage to dissipated energy evolution for a moderate differential stress load case that produces continuous simple propagation. The cumulative global pattern shows a series of stair-stepping events reflecting buildup-rupture cycles. Intervals with a steep slope (orange arrow, Figure 6) reflect arrest and buildup stages where damage accumulates slower than energy is dissipated. Intervals with a shallow slope (blue arrow, Figure 6) represent growth stages where damage spreads abruptly. Energy jumps are associated with high-velocity ruptures that manifest as a short burst of damage. Note that the steep slopes in Figure 6 develop over a few time points (each small dot is a 0.001-s increment), whereas the shallowly sloped growth stages comprise many time points. The behavior is not only consistent for the macroscopic rupture-arrest pattern but also holds locally as shown by the zoomed-in inset in Figure 6.

Whether propagation is stable or unstable is determined by small early ruptures that initiate from the fracture tip. Forward propagation of pre-rupture damage preconditions the region ahead of the main fracture path, reducing the tendency for subsequent large, unstable ruptures. If the initial rupture events are unstable and fail more energetically, the resulting damage cloud extends further (Buseti, 2009) and potential branch sites initiate, but only weakly develop, and then are bypassed as consecutive ruptures extend with the propagating damage front (Figure 4A, C; c in Figure 5).

Conversely, under more stable conditions, damping of early kinetic oscillations occurs as a result of incremental yielding (Buseti, 2009). Thus, a product of the more stable early ruptures is that the damage accumulated during the first buildup stages is more localized, leading to the buildup of more strongly developed sets of failed branches (b in Figure 4B). This early complex pattern accommodates strain within a few damage branches and their associated damage clouds, and thus, no clear damage preconditioning occurs ahead of the main fracture path. Consequently, despite the more stable loading conditions, the formation of off-plane damage during the slowly advancing buildup stages may increase the tendency for overall instability. Subsequent ruptures are more unstable and punctuated, and the resulting damage corridor is more complex and irregular (Figure 4B; a and d in Figure 5).

## SUMMARY

We developed FE simulations of damage fracturing at the tip of a hydraulic fracture and analyzed the morphology and dynamic propagation. The models are consistent with field observations and experimental data, indicating the following:

1. The evolving local stress state strongly affects the stress path (e.g., how close the rock layer is to failure) and controls the mode and distribution of local failure (tensile, shear, or mixed mode).
2. A uniform pressure distribution in the DF creates an elliptical fracture shape and increases the shear contribution at the fracture tip. This effect is more pronounced for low tectonic stress ratios. A nonuniform pressure distribution results in a cusped fracture that leads to tensile-dominated damage.

The simulations also provide new insights into transient damage processes that are likely to occur during hydraulic fracturing:

1. Transient damage fracture propagation occurs as the elastic energy stored from HF pressurizing is slowly dissipated during damage buildup

stages corresponding to local strain hardening and is released unstably in fracture rupture events.

2. Stable propagation via short controlled ruptures occurs when the damage is spatially constrained so that it preconditions the potential fracture path for subsequent propagation. Unstable propagation happens if the zones of damage transference are nonideally linked and buildup stages and ruptures occur out of sequence systemwise.
3. The simulations indicate that it is unlikely that an idealized, simple HF shape could be sustained for any extended distance in reservoir rocks under in-situ conditions where fluid lag processes are active. A more likely configuration is the development of a complex, damaged fracture network.

## APPENDIX 1: FINITE ELEMENT CONTINUUM DAMAGE MODEL

Our models implement a finite element (FE) damage scheme (de Borst and Nauta, 1985; Bazant, 1986) developed by Lubliner et al. (1989) and later modified by Lee and Fenves (1998) to include cyclic loading and compressive and tensile behavior. The material model is included in Abaqus as concrete damage plasticity. The material elastic properties,  $D$ , and effective stress,  $\sigma$ , in the host medium depend on the amount of damage accumulated through microcracking in compression and tension (Lee and Fenves, 1998):

$$D = D(\kappa) = l - (l - D_t)(l - D_c) \quad (3a)$$

$$\sigma = (l - D)\sigma; \sigma = (l - D)E_0:(\varepsilon - \varepsilon^p) \quad (3b)$$

where the material matrix,  $D$ , has a tensile and compressive component  $D_t$  and  $D_c$ ,  $\kappa$  is the damage variable,  $\varepsilon$  and  $\varepsilon^p$  are the scalar elastic and plastic strains,  $\sigma$  is the stress tensor, and  $E_0$  is the original elastic stiffness. Damage increase caused by microcracking is proportionate to the dissipated fracture energy density,  $G$ , normalized over a localization zone with a characteristic length,  $l$ :

$$\kappa_N = l/g_N \int_0^{\varepsilon^p} \sigma_N(\varepsilon^p) d\varepsilon^p \quad (4a)$$

$$g_N = \int_{-\infty}^0 \sigma_N(\varepsilon^p) d\varepsilon^p \quad (4b)$$

$$g_N = G_N/l_N \quad (4c)$$

The normalized fracture energy,  $g_N$ , in equation 4b is analogous to the energy definition for the shielding zone of the

cohesive crack model, with the exception that the constitutive relationship in equation 4b is based on plastic-damage theory (see Lubliner et al., 1989). This scheme is useful in our investigations for a few reasons. First, the continuum damage avoids the limitations of the crack-tip approaches and the entire model domain is capable of induced failure, propagation of multiple cracks, and self-interaction. Second, because the damage model is compatible with fracture-mechanics theory, many of the same interpretation techniques are possible. Specifically, we compared how energy is dissipated in the system for different loading conditions. Third, the FE implementation permits simulation of fracture propagation based on the equivalent crack concept, which states that a length-scaled damage zone that is thermodynamically equivalent to a crack and vice versa exists. For a more thorough discussion on the equivalence of fracture and damage energy, refer to Mazars and Pijaudier-Cabot (1996). A discrete fracture is represented by a path of elements that are completely damaged and have no strength. Finally, we are able to use the Abaqus software to model the rheology as well as to solve the complex mechanics involved in transient nonlinear propagation. We chose a widely used commercial FE code for some practical reasons, in particular, that the software interface did not require additional programming or the use of other add-ons and that some of Abaqus help resources and professional publications are available online.

## APPENDIX 2: EXPLICIT DYNAMIC FINITE ELEMENT SOLUTION

To solve the problem, we use the explicit dynamic FE procedure of Abaqus/Explicit. The explicit technique is popular for solving a diverse range of nonlinear dynamics problems. The technique incrementally solves for the transient physical behavior of the problem and is designed to handle extreme local instability. Thus, it is well suited to simulate transient propagation of damage and complex fracture morphologies. A brief discussion follows on the explicit technique as applied in Abaqus (Abaqus theory manual; Simulia, 2010b). For the general concepts of FE, we refer the reader to Fish and Belytchko (2007) and Reddy (2004, 2007).

The basic FE procedure for structural analysis is to find an approximate discretized solution for displacement  $u(x)$  for the differential equation (here shown in 1-D for clarity):

$$-d/d_x(a[d_u/d_x]) + c_u - f = 0 \text{ for } 0 < x < L \quad (5)$$

Equation 5 is simply Hooke's law in differential form, where  $f$  is the vector of external forces;  $a = a(x)$  reflects the material property (e.g.,  $a = EA$ , Young's modulus  $x$  area);  $c = c(x)$  is an environmental variable, for instance, a penalty constraint; and  $\varepsilon = d_u/d_x$ . A series of mathematical operations allows equation 5 to be recasted in algebraic form in terms of matrix coefficients:

$$Ku - F = 0 \quad (6)$$

The coefficient  $\mathbf{K}$  is referred to as the stiffness matrix,  $u$  is the displacement vector, and  $F$  is the external force vector. The global  $\mathbf{K}$  contains the material properties and shape functions (linear or quadratic) assembled over the entire mesh. The implicit FE technique (e.g., Abaqus/Standard) formulates the  $3 \times 3$  stiffness matrix  $K_{ij}^e$  for each element to assemble the global matrix  $\mathbf{K}$ , which is then inverted to find the nodal displacement values,  $u$ . For nonlinear problems, the computation must be divided into many solution-time increments, and each increment may take several iterations to converge upon a stable solution. If large changes in material properties, numerous evolving contacts, or extreme deformations are observed, it may be impossible to achieve convergence. Alternatively, the explicit procedure solves equation 5 using sufficiently small physical-time increments on an element-by-element basis and, consequently, does not require full matrix inversion and iterative convergence. The procedure is based on integrating the equations of motion ( $F = m \times a$ , where  $F$  = force,  $m$  = mass, and  $a$  = acceleration) and thus considering dynamic effects. Modification of equation 6 yields

$$\mathbf{M}\ddot{u} + \mathbf{K}u - F = 0 \quad (7)$$

where  $\mathbf{M}$  is the diagonal mass matrix and  $\ddot{u}$  is the acceleration vector. The size of the stable time increment is determined by the characteristic element dimension,  $L_e$ , and the smallest dilatational wave speed of the material,  $c_d$ , for all elements in the mesh.

$$\Delta t = \min(L_e/c_d) \quad (8a)$$

$$c_d = ([\lambda + 2\mu]/\rho)^{1/2} \quad (8b)$$

where  $\lambda$  and  $\mu$  are effective Lamé's constants and  $\rho$  is the density of the material. In short, small elements, high material stiffness, low material density, and large applied loads reduce numerical stability, decrease the time increment, and increase the computation time. The equations of motion are solved using a time integration scheme, where  $i$  is the time increment:

$$\int_{t_i}^{t_{i+1}} F(t)dt = ([1 - \theta]F_i + \theta F_{i+1})\Delta t \quad (9a)$$

Abaqus/Explicit uses a central difference rule (the time mid-increment parameter  $\theta = 1/2$ ), so that the equations of motion become

$$u^{(i+1)} = u^{(i)} + \Delta t^{(i+1)}\dot{u}^{(1+1/2)} \quad (9b)$$

$$\dot{u}^{(i+1/2)} = \dot{u}^{(i-1/2)} + 1/2(\Delta t^{(i+1)} + \Delta t^{(i)})\ddot{u}^{(i)} \quad (9c)$$

$$\ddot{u}^{(i)} = \mathbf{M}^{-1}(F^{(i)} - \mathbf{K}u^{(i)}) \quad (9d)$$

The solution for each increment is achieved using  $u^{(i)}$  and  $\dot{u}^i$  at the state of the previous increment to invert the diagonal mass matrix in equation 9d at the beginning of the

subsequent increment to compute the acceleration  $\ddot{u}^{(i+1)}$ . Integrating twice gives the primary displacement variables at the nodes of each element for the current time increment. The post-processor of Abaqus then uses the nodal displacements to compute the secondary variables, that is, stress and strain, at a single integration point in each element. The shape functions interpolate the values within each element. Note that, in the present models for the elastic-plastic damage material, the parameter  $a$  in equation 5 is a function that varies spatially and evolves over time depending on plastic strain, such that  $\mathbf{K} = f(u_{ij}[t], e^p[t])$ . Based on the plastic strain at each increment, the damage parameters in tension and compression are then calculated and are used to update the material stiffness and the shape of the yield surface for each element.

## REFERENCES CITED

- Backers, T., S. Stanchits, and G. Dresen, 2005, Tensile fracture propagation and acoustic emission activity in sandstone: The effect of loading rate: *International Journal of Rock Mechanics and Mining Sciences*, v. 42, no. 7–8, p. 1094–1101, doi:10.1016/j.ijrmms.2005.05.011.
- Baer, G., and Z. Reches, 1991, Mechanics of emplacement and tectonic implications of the Ramon dike systems, Israel: *Journal of Geophysical Research*, v. 96, no. B7, p. 11,895–11,910.
- Baer, G., M. Beyth, and Z. Reches, 1994, Dikes emplaced into fractured basement, Timna igneous complex, Israel: *Journal of Geophysical Research*, v. 99, no. B12, p. 24,039–24,050.
- Barenblatt, G., 1962, The mathematical theory of equilibrium crack in the brittle fracture: *Advances in Applied Mechanics*, v. 7, p. 55–125.
- Bazant, Z. P., 1986, Mechanics of distributed cracking: *Applied mechanics reviews: American Society of Mechanical Engineers*, v. 39, p. 675–705.
- Bobich, J. K., 2005, Experimental analysis of the extension to shear fracture transition in Berea Sandstone: Master's thesis, Texas A&M University, College Station, Texas, 52 p.
- Busetti, S., 2009, Fracturing of layered reservoir rocks: Ph.D. dissertation, University of Oklahoma, Norman, Oklahoma, 256 p.
- Busetti, S., and Z. Reches, 2007, Formation of network fractures during hydraulic fracturing of the Barnett Shale, a tight gas shale with preexisting fractures (abs.): *Eos Transactions of the American Geophysical Union, Fall Meeting Supplement T42C-04*, v. 88, no. 52, 330 p.
- Busetti, S., K. Mish, and Z. Reches, 2012, Damage and plastic deformation of reservoir rocks: Part 1. Damage fracturing: *AAPG Bulletin*, v. 96, p. 1687–1709.
- Chang, S. H., and C. I. Lee, 2004, Estimation of cracking and damage mechanisms in rock under triaxial compression by moment tensor analysis of acoustic emission: *International Journal of Rock Mechanics and Mining Sciences*, v. 41, p. 1069–1086, doi:10.1016/j.ijrmms.2004.04.006.
- Chen, Z. H., L. G. Tham, M. R. Yeung, and H. Xie, 2006, Confinement effects for damage and failure of brittle

- rocks: *International Journal of Rock Mechanics and Mining Sciences*, v. 43, p. 1262–1269, doi:10.1016/j.ijrmms.2006.03.015.
- Cooke, M. L., and D. D. Pollard, 1996, Fracture propagation paths under mixed-mode loading within rectangular blocks of polymethacrylate: *Journal of Geophysical Research*, v. 101, no. B2, p. 3387–3400, doi:10.1029/95JB02507.
- Cosgrove, J. W., and T. Engelder, eds., 2001, *The initiation, propagation, and arrest of joints and other fractures: Geological Society (London) Special Publication*, v. 231.
- De Borst, R., and P. Nauta, 1985, Nonorthogonal cracks in a smeared finite element model: *Engineering Computing*, v. 117, p. 35–46, doi:10.1108/eb023599.
- Delaney, P. T., and A. E. Gartner, 1997, Physical processes of shallow mafic dike emplacement near the San Rafael swell, Utah: *Geological Society of America Bulletin*, v. 109, no. 9, p. 1177–1192, doi:10.1130/0016-7606(1997)109<1177:PPOSMD>2.3.CO;2.
- Delaney, P. T., D. D. Pollard, J. I. Zioney, and E. H. McKee, 1986, Field relations between dikes and joints: Emplacement processes and paleostress analysis: *Journal of Geophysical Research*, v. 91, p. 4920–4938, doi:10.1029/JB091iB05p04920.
- Elder, C. H., 1977, Effects of hydraulic stimulation on coalbeds and associated strata: United States Department of the Interior, Bureau of Mines, Report of Investigations 8260, 20 p.
- Fast, R. E., A. S. Murer, and R. S. Timmer, 1994, Description and analysis of cored hydraulic fractures, Lost Hills field, Kern County, California: *Society of Petroleum Engineers Production and Facilities*, v. 9, no. 2, p. 107–114.
- Fish, J., and T. Belytchko, 2007, *A first course in finite elements: West Sussex, England, Wiley*, 336 p.
- Hart, D. J., and H. F. Wang, 1995, Laboratory measurements of a complete set of poroelastic moduli for Berea Sandstone and Indiana limestone: *Journal of Geophysical Research*, v. 100, no. B9, p. 17,741–17,751.
- Hubbert, M. K., and D. G. Willis, 1957, Mechanics of hydraulic fracturing: *Transactions of the American Institute of Mining, Metallurgical, and Petroleum Engineers* 210, p. 153–68.
- Irwin, G. R., 1958, Fracture, in *Handbuch der Physik 6: Berlin, Springer-Verlag*, p. 551–590.
- Ishida, T., Q. Chen, M. Yoshiaki, and J. C. Roegiers, 2004, Influence of viscosity on the hydraulic fracturing mechanism: *Journal of Energy Resources Technology*, v. 126, p. 190–200, doi:10.1115/1.1791651.
- Katz, O., and Z. Reches, 2004, Microfracturing, damage, and failure of brittle granites: *Journal of Geophysical Research*, v. 109, p. B01206, doi:10.1029/2002JB001961.
- Lee, J., and G. L. Fenves, 1998, Plastic-damage model for cyclic loading of concrete structures: *Journal of Engineering Mechanics*, v. 124, p. 892–900, doi:10.1061/(ASCE)0733-9399(1998)124:8(892).
- Levi, T., R. Weinberger, and Y. Eyal, 2009, Decay of dynamic fracturing based on three-dimensional measurements of clastic-dike geometry: *Journal of Structural Geology*, v. 31, p. 831–841, doi:10.1016/j.jsg.2009.06.002.
- Lubliner, J., J. Oliver, S. Oller, and E. Onate, 1989, A plastic-damage model for concrete: *International Journal of Solids and Structures*, v. 25, no. 3, p. 299–326, doi:10.1016/0020-7683(89)90050-4.
- Lyakhovskiy, V., Z. Reches, R. Weinberger, and T. E. Scott, 1997, Nonlinear elastic behavior of damaged rocks: *Geophysics Journal International*, v. 130, p. 157–166, doi:10.1111/j.1365-246X.1997.tb00995.x.
- Mazars, J., and G. Pijaudier-Cabot, 1996, From damage to fracture mechanics and conversely: A combined approach: *International Journal of Solids and Structures*, v. 33, p. 3327–3342, doi:10.1016/0020-7683(96)00015-7.
- Menendez, B., W. Zhu, and T. Wong, 1996, Micromechanics of brittle faulting and cataclastic flow in Berea Sandstone: *Journal of Structural Geology*, v. 18, p. 1–16, doi:10.1016/0191-8141(95)00076-P.
- Ostensen, R. W., 1983, Microcrack permeability in tight gas sandstone: *Society of Petroleum Engineers Journal*, v. 23, no. 6, p. 919–927.
- Papanastasiou, P., 2002, Hydraulic fracturing: Basic concepts and numerical modeling: Alliance of Laboratories in Europe for Research and Technology: <http://alert.epfl.ch/Archive/ALERT2006/pdf/7%20Papanastasiou%20P%20Hydraulic%20fracturing.pdf> (accessed September 24, 2009).
- Pollard, D. D., 1978, Forms of hydraulic fractures as deduced from field studies of sheet intrusions: *Proceedings of the 19th U.S. Rock Mechanics Symposium, Stateline, Nevada, May 1–3*, v. 1, no. 19, p. 1–9.
- Ramsey, J. M., and F. M. Chester, 2004, Hybrid fracture and the transition from extension fracture to shear fracture: *Nature*, v. 428, p. 63–66, doi:10.1038/nature02333.
- Reches, Z., and D. Lockner, 1994, Nucleation and growth of faults in brittle rocks: *Journal of Geophysical Research*, v. 99, no. B9, p. 18,159–18,173.
- Reddy, J. N., 2004, *Introduction to the finite element method: Columbus, Ohio, McGraw-Hill*, 912 p.
- Reddy, J. N., 2007, *An introduction to nonlinear finite element analysis: New York, Oxford University Press*, 463 p.
- Rice, J. R., 1968, A path-independent integral and the approximate analysis of strain concentration by notches and cracks: *Journal of Applied Mechanics*, v. 35, p. 379–386, doi:10.1115/1.3601206.
- Roth, M., and A. Thompson, 2009, Fracture interpretation in the Barnett Shale using macro- and microseismic data: *First Break*, v. 27, no. 4, p. 83–88.
- Rutledge, J. T., W. S. Phillips, and M. J. Mayerhofer, 2004, Faulting induced by forced fluid injection and fluid flow forced by faulting: An interpretation of hydraulic-fracture microseismicity, Carthage Cotton Valley gas field, Texas: *Bulletin of the Seismological Society of America*, v. 94, no. 5, p. 1817–1,830, doi:10.1785/012003257.
- Sagy, A., Z. Reches, and I. Roman, 2001, Dynamic fracturing of rock fragmentation and joint density: Field and experimental observations: *Journal of Structural Geology*, v. 23, p. 1223–1239.
- Sasaki, S., 1998, Characteristics of microseismic events during hydraulic fracturing experiments at the Hijiori hot dry rock geothermal energy site, Yamagata, Japan: *Tectonophysics*, v. 289, p. 171–188, doi:10.1016/S0040-1951(97)00314-4.

- Sim, Y., 2004, Mechanics of complex hydraulic fractures in the Earth's crust: Ph.D. dissertation, Georgia Institute of Technology, Atlanta, Georgia, 324 p.
- Simpson, G., Y. Gueguen, and F. Schneider, 2001, Permeability enhancement due to microcrack dilatancy in the damage regime: *Journal of Geophysical Research*, v. 106, no. B3, p. 3999–4016, doi:[10.1029/2000JB900194](https://doi.org/10.1029/2000JB900194).
- Simulia, 2010a, Abaqus explicit user's manual, version 6.7: Providence, Rhode Island, Dassault Systemes.
- Simulia, 2010b, Abaqus theory manual, version 6.7: Providence, Rhode Island, Dassault Systemes.
- Thompson, R. M., 1986, Physics of fracture, *in* H. Ehrenreich and D. Turnbull, eds., *Solid-state physics*, v. 39, p. 1–129.
- Van Dam, C. J., C. J. De Pater, and R. Romijn, 1999, Reopening of dynamic fractures in laboratory experiments: *International Congress on Rock Mechanics*, Paris, France, August 25–28, p. 792–794.
- Warpinski, N. R., and L. W. Teufel, 1987, Influence of geologic discontinuities on hydraulic fracture propagation: *Journal of Petroleum Technology*, v. 39, no. 2, p. 209–220.
- Warpinski, N. R., J. C. Lorenz, P. T. Branagan, F. R. Myal, and B. L. Gall, 1993, Examination of a cored hydrofracture in a deep gas well: *Society of Petroleum Engineers Production and Facilities*, v. 8, no. 3, p. 150–158.
- Weinberger, R., Z. Reches, A. Eidelman, and T. E. Scott, 1994, Tensile properties of rocks in four-point beam tests under confining pressure, *in* P. P. Nelson and S. E. Laubach, eds., *Rock mechanics models and measurements: Challenges from industry: Proceedings of the 1st North American Rock Mechanics Symposium*, University of Texas at Austin: Rotterdam, Balkema, p. 435–442.
- Weinberger, R., V. Lyakhovskiy, G. Baer, and A. Agnon, 2000, Damage zones around en echelon dike segments in porous sandstone: *Journal of Geophysical Research*, v. 105, no. B2, p. 3115–3133, doi:[10.1029/1999JB900361](https://doi.org/10.1029/1999JB900361).
- Wu, R., 2006, Some fundamental mechanisms of hydraulic fracturing: Ph.D. dissertation, Georgia Institute of Technology, Atlanta, Georgia, 280 p.
- Zhou, J., M. Chen, Y. Jin, and G. Zhang, 2008, Analysis of fracture propagation behavior and fracture geometry using a triaxial fracturing system in naturally fractured reservoirs: *International Journal of Rock Mechanics and Mining Science*, v. 45, no. 7, p. 1143–1152, doi:[10.1016/j.ijrmms.2008.01.001](https://doi.org/10.1016/j.ijrmms.2008.01.001).
- Zhu, W., and T. Wong, 1999, Network modeling of the evolution of permeability and dilatancy in compact rock: *Journal of Geophysical Research*, v. 104, p. 2963–2971, doi:[10.1029/1998JB900062](https://doi.org/10.1029/1998JB900062).
- Zoback, M., and J. Byerlee, 1975, The effect of microcrack dilatancy on the permeability of Westerly granite: *Journal of Geophysical Research*, v. 80, no. 5, p. 752–755, doi:[10.1029/JB080i005p00752](https://doi.org/10.1029/JB080i005p00752).